Exp. Theo. NANOTECHNOLOGY 10 (2026) 627-644 https://doi.org/10.56053/10.2.627

Scalable synthesis of Al-doped CuO ceramic nanoparticles using a citrate-based sol-gel approach

Mojahid M. Najim[1], *Ban A. Yousif*[2], *Mohammed RASHEED*[3,*]

[1] Nanomaterials Research Center, University of Anbar, Ramadi, Iraq
[2] Department of Applied Science, University of Technology- Iraq, Baghdad 10066, Iraq
[3] College of Production Engineering & Metallurgy, University of Technology- Iraq, Baghdad, Iraq
[*]) Email: rasheed.mohammed40@yahoo.com

Received 7/2/2026, *Received in revised form* 23/3/2026, *Accepted* 29/3/2026, *Published* 15/4/2026

Al-doped CuO nanoparticles with Al concentrations of 0%, 1%, 3%, and 5% are successfully synthesized via a citrate-based sol–gel method followed by sintering at 1000 °C. X-ray diffraction (XRD) analysis confirmed the formation of single-phase monoclinic CuO (space group C2/c), with characteristic peaks indexed to the (110), (−111), (111), (−113), (−311), and (004) planes. A systematic shift of diffraction peaks toward higher 2θ values and a reduction in crystallite size from 17.74 nm (S1) to 15.30 nm (S4) are observed, indicating lattice contraction due to Al^{3+} substitution. FTIR spectra revealed characteristic Cu–O vibrations in the range of 500–600 cm^{-1}, along with enhanced O–H stretching bands (~3200–3500 cm^{-1}), confirming increased surface hydroxylation with Al doping. Raman analysis showed typical CuO modes at ~298, ~348, and ~633 cm^{-1}, with noticeable peak broadening and shifts in doped samples, indicating increased lattice disorder. Thermal analysis (TGA/DTG/DSC) demonstrated multi-stage weight loss, with total mass loss increasing from ~4.5% (S1) to ~6.9% (S4). DTG peaks shifted from ~150°C to ~135°C (moisture removal) and from ~380°C to ~330°C (decomposition), indicating reduced thermal stability with increasing Al content. Archimedes measurements showed a decrease in apparent porosity from ~25% (S1) to ~15% (S4) and an increase in bulk density from ~4.7 g/cm^3 to ~5.3 g/cm^3, confirming enhanced densification. Morphological analysis indicated improved particle uniformity with increasing Al concentration. These results demonstrate that Al doping effectively modifies the structural, thermal, and microstructural properties of CuO, making the materials suitable for advanced applications in catalysis, sensing, and electronic devices. CP-OES analysis showed a composition-dependent Cu^{2+} ion release, with the lowest release at 3% Al doping, suggesting optimal structural stability among the investigated samples.

Exp. Theo. NANOTECHNOLOGY 10 (2026) 627-644

Keywords: Al-doped CuO nanoparticles; Citrate sol–gel method; XRD; Ceramic.

1. INTRODUCTION

Copper oxide (CuO) nanoparticles have attracted significant attention due to their unique structural, optical, and electronic properties, making them suitable for a wide range of technological applications [1-5]. CuO is a p-type semiconductor with a narrow band gap, which enables its use in sensors, catalysis, energy storage, and optoelectronic devices [6-10]. In recent years, various synthesis techniques such as hydrothermal, precipitation, and sol–gel methods have been explored to produce CuO nanoparticles with controlled size and morphology [11-15]. Among these, the citrate-based sol–gel method has emerged as a simple, cost-effective, and scalable approach that ensures high homogeneity and fine particle distribution [16,17]. Despite the extensive research on CuO nanoparticles, achieving precise control over their structural and functional properties remains a challenge [18-20]. Pure CuO often suffers from limitations such as poor conductivity, limited surface activity, and restricted tunability of its band structure [21,22]. These drawbacks hinder its performance in advanced applications such as gas sensing, photocatalysis, and electronic devices [23,24]. Therefore, modifying CuO through doping has become an effective strategy to overcome these limitations and enhance its performance [25]. Doping with trivalent elements such as aluminum (Al^{3+}) has been widely investigated as a means to tailor the structural, electrical, and optical properties of CuO nanoparticles [26,27]. The substitution of Cu^{2+} ions with smaller Al^{3+} ions can induce lattice distortion, modify defect concentrations, and influence grain size and crystallinity [28-30]. These changes can significantly affect the material's conductivity, band gap, and surface reactivity. However, there is still a lack of systematic studies focusing on low-concentration Al doping levels (such as 1–5 mol%) synthesized via a citrate-based sol–gel route, particularly in relation to their structural evolution and phase behavior [31-33]. The research gap lies in the limited understanding of how controlled Al doping at low concentrations influences the crystallographic structure and phase purity of CuO nanoparticles prepared using scalable synthesis methods [34,35]. Moreover, inconsistencies in synthesis parameters and lack of comparative analysis across different doping levels make it difficult to establish clear structure–property relationships [36,37]. Addressing this gap is essential for optimizing CuO-based materials for practical applications [38]. Al-doped CuO nanoparticles have potential applications in various fields, including gas sensors, photocatalysts, lithium-ion batteries, and antimicrobial coatings [39, 40]. The improved electrical conductivity and enhanced surface activity resulting from doping can significantly boost the performance of these materials [41, 42]. Additionally, the ability to tune material properties through controlled doping makes Al-doped CuO a promising candidate for next-generation functional nanomaterials [43-45]. The novelty of this work lies in the systematic investigation of CuO nanoparticles doped with different concentrations of aluminum (0%, 1%, 3%, and 5%) synthesized via a citrate-based sol–gel method, followed by high-temperature sintering at 1000 °C. This study provides a comparative analysis of structural changes induced by Al incorporation under consistent synthesis conditions, offering insights into doping-induced modifications. The main objectives of this study are to synthesize pure and Al-doped CuO nanoparticles using a scalable sol–gel technique, to analyze the effect of varying Al concentrations on the structural properties, and to establish correlations between doping levels and material characteristics. However, this study is limited to structural investigation and does not include detailed electrical or optical characterization, which may be explored in future work. In this paper, CuO and Al-doped CuO nanoparticles with varying doping concentrations are synthesized using a citrate-based sol–gel method, and their structural properties are systematically investigated to understand the influence of Al incorporation.

2. MATERIALS AND METHODS

2.1. Materials

Copper nitrate trihydrate ($Cu(NO_3)_2 \cdot 3H_2O$, MW = 241.60 g·mol^{-1}, purity ≥ 99%, Sigma-Aldrich) is used as the copper precursor. Aluminum nitrate nonahydrate ($Al(NO_3)_3 \cdot 9H_2O$, MW = 375.13 g·mol^{-1}, purity ≥ 98%, Sigma-Aldrich) served as the aluminum dopant source. Citric acid ($C_6H_8O_7$, MW = 192.12 g·mol^{-1}, purity ≥ 99.5%, Sigma-Aldrich) is employed as a chelating and complexing agent in the sol–gel process. Deionized water is used as the solvent throughout the synthesis. Al-doped CuO samples with different aluminum concentrations are prepared and the samples are labeled as S1, S2, S3, and S4 corresponding to 0%, 1%, 3%, and 5% Al-doped CuO, respectively.

2.2. Preparation of Al-doped CuO NPs

Al-doped CuO nanoparticles are synthesized using a citrate-based sol–gel method. Initially, 24.16 g of $Cu(NO_3)_2 \cdot 3H_2O$ (0.1 mol) is dissolved in approximately 100 mL (≈100 g) of deionized water under continuous magnetic stirring to obtain a homogeneous solution for the undoped sample (S1). For the doped samples, the total metal ion concentration is fixed at 0.1 mol, and appropriate amounts of aluminum nitrate are introduced. Specifically, for S2 (1% Al-doped CuO), 23.92 g of $Cu(NO_3)_2 \cdot 3H_2O$ (0.099 mol) and 0.38 g of $Al(NO_3)_3 \cdot 9H_2O$ (0.001 mol) are dissolved in 100 mL (≈100 g) of deionized water. For S3 (3% Al-doped CuO), 23.44 g of $Cu(NO_3)_2 \cdot 3H_2O$ (0.097 mol) and 1.13 g of $Al(NO_3)_3 \cdot 9H_2O$ (0.003 mol) are used, while for S4 (5% Al-doped CuO), 22.95 g of $Cu(NO_3)_2 \cdot 3H_2O$ (0.095 mol) and 1.88 g of $Al(NO_3)_3 \cdot 9H_2O$ (0.005 mol) are dissolved in the same volume of deionized water. Citric acid is then added gradually to each mixed nitrate solution in a 1:1 molar ratio with total metal ions; thus, 19.21 g of citric acid (0.1 mol) is added to each sample under constant stirring to act as a chelating agent and ensure homogeneous distribution of Cu^{2+} and Al^{3+} ions. The resulting solution is heated at 80 °C using a magnetic stirrer until a clear and stable sol is formed. Continued heating at the same temperature led to solvent evaporation and gradual transformation of the sol into a viscous gel. Upon further heating, the gel underwent drying and self-combustion, producing a dark, porous precursor powder due to the decomposition of nitrate–citrate complexes and the evolution of gaseous by-products such as H_2O, CO_2, and nitrogen oxides. The obtained powder is cooled to room temperature and then ground thoroughly using an agate mortar and pestle to achieve fine and uniform particle size. The powder is further dried to remove residual moisture and reground to improve homogeneity. The prepared powders are subsequently compacted into pellets using a hydraulic press. Finally, the pellets are sintered at 1000 °C in air, followed by natural cooling to room temperature. This high-temperature treatment enhanced crystallinity, phase formation, and densification of the Al-doped CuO nanoparticles. The final samples are labeled as S1, S2, S3, and S4 corresponding to 0%, 1%, 3%, and 5% Al-doped CuO, respectively, for further characterization.

2.3. Characterization

The structural, morphological, and thermal properties of pure and Al-doped CuO samples are investigated using various characterization techniques. X-ray diffraction (XRD) analysis is carried out to determine the crystal structure, phase purity, and crystallite size of the synthesized samples. The measurements are performed using an X-ray diffractometer (e.g., PANalytical X'Pert PRO, Malvern PANalytical, Netherlands) with Cu Kα radiation (λ = 1.5406 Å), operated at 40 kV and 30 mA. The diffraction patterns are recorded over a 2θ range of 10°–90° with a step size of 0.02°. Fourier transform infrared (FTIR) spectroscopy is used to identify functional groups and chemical bonding. The spectra are recorded using an FTIR spectrometer (e.g., PerkinElmer Spectrum Two, USA) in the range of 400–4000 cm^{-1}, with a resolution of 0.1 cm^{-1}. Raman spectroscopy is employed to analyze vibrational modes and confirm the crystal structure. The measurements are performed using a Raman

spectrometer (e.g., Renishaw inVia Raman microscope, UK) with a laser excitation wavelength of 532 nm, and spectra are collected over a range of 100–1000 cm^{-1}. The density and porosity of the samples are determined using the Archimedes method with distilled water as the immersion medium. Bulk density and apparent porosity are calculated based on dry, soaked, and suspended weights. Thermogravimetric analysis (TGA) and derivative thermogravimetry (DTG) are conducted to evaluate thermal stability and decomposition behavior using a thermal analyzer (e.g., TA Instruments Q500, USA). The measurements are carried out in the temperature range of room temperature to 800 °C at a heating rate of 10 °C/min under a nitrogen atmosphere. Differential scanning calorimetry (DSC) is performed to study thermal transitions using a DSC instrument (e.g., TA Instruments Q2000, USA) over a temperature range of 25–800 °C at a heating rate of 10 °C/min. These characterization techniques collectively provided comprehensive information on the structural, vibrational, morphological, and thermal properties of the synthesized Al-doped CuO nanoparticles. The release of Cu^{2+} ions from pure and Al-doped CuO nanoparticles is measured using ICP-OES (PerkinElmer Optima 8000, USA) following one week of immersion.

3. RESULTS AND DISCUSSION

3.1. Bulk density and apparent porosity

The variation of apparent porosity (%) and bulk density (g/cm^3) of pure CuO (S1) and Al-doped CuO samples (S2: 1%, S3: 3%, and S4: 5%) determined using the Archimedes method is presented in Figure 1. As shown in Figure 1, the apparent porosity decreases progressively with increasing Al content, whereas the bulk density exhibits an opposite trend, indicating enhanced densification of the samples. For the undoped sample (S1, 0% Al), the apparent porosity is the highest (≈25%), while the bulk density is the lowest (≈4.7 g/cm^3), as illustrated in Figure 1. This suggests that the pure CuO sample possesses a relatively porous structure with less compact grain packing. The high porosity can be attributed to incomplete densification during the sintering process. With the addition of 1% Al (S2), a reduction in apparent porosity (≈22–23%) is observed along with an increase in bulk density (≈4.9 g/cm^3), as clearly seen in Figure 1. This indicates that Al doping improves particle packing and enhances densification. The presence of Al^{3+} ions promote diffusion processes, leading to a reduction in pore volume. As the Al content increases to 3% (S3), the apparent porosity further decreases (≈19–20%), while the bulk density increases to approximately 5.1 g/cm^3, as shown in Figure 1. This reflects improved grain connectivity and a more compact microstructure. The reduction in pore size and number contributes to the observed increase in density. At the highest doping level, 5% Al (S4), the apparent porosity reaches its minimum value (≈15–16%), and the bulk density attains its maximum value (≈5.3 g/cm^3), as illustrated in Figure 1. This indicates that S4 exhibits the highest degree of densification and the lowest pore content among all samples. As observed in Figure 1, increasing Al concentration leads to a systematic decrease in porosity and a corresponding increase in bulk density [46, 47]. This behavior can be attributed to the smaller ionic radius of Al^{3+} compared to Cu^{2+}, which enhances lattice packing and diffusion during sintering. Consequently, Al doping improves the structural compactness and densification of CuO ceramics [48-50].

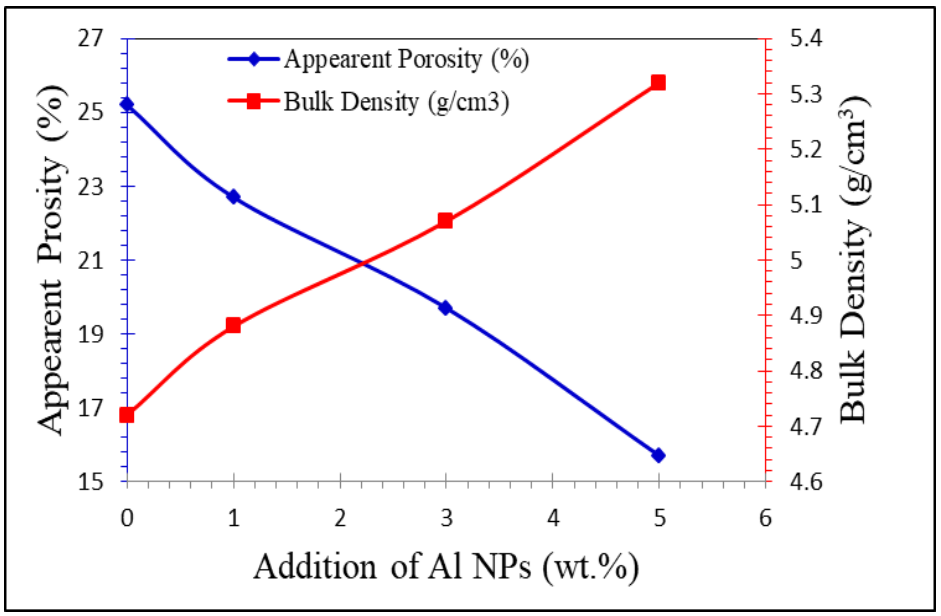

Figure 1 Variation of apparent porosity (%) and bulk density (g/cm³) of pure CuO (S1) and Al-doped CuO samples (S2: 1%, S3: 3%, and S4: 5%) as a function of Al content.

3.2. XRD analysis

Based on Figure 2 and Table 1, all the samples, namely S1 (0% Al-doped CuO), S2 (1% Al-doped CuO), S3 (3% Al-doped CuO), and S4 (5% Al-doped CuO), can be interpreted as having a monoclinic CuO (tenorite) crystal structure. The observed diffraction peaks are consistent with standard CuO and indicate that Al addition does not change the basic host structure, but instead causes slight modifications in peak position, peak width, and crystallite size. This means that Al is incorporated into the CuO lattice or influences the lattice locally without producing a major structural transformation in the studied range. The diffraction data therefore support the formation of single-phase Al-doped CuO, with no dominant secondary phase visible within the detection limit of the presented pattern. The diffraction peaks may be indexed to standard monoclinic CuO, commonly matched with JCPDS/PDF card No. 48-1548 or equivalent CuO tenorite reference files reported in the literature. The main reflections used in Table 1 are centered approximately at 32.5°, 35.5°, 38.7°, 61.5°, 66.2°, and 75.1° for the undoped sample, corresponding respectively to the planes (110), (-111), (111), (-113), (-311), and (004). In the Al-doped samples, these reflections shift slightly toward higher 2θ values, for example from 32.50° in S1 to 32.66° in S4, from 35.50° to 35.66°, and from 38.70° to 38.86°. Similar small shifts are also observed for the higher-angle peaks. These systematic shifts suggest a slight contraction of the CuO lattice, which is reasonable because Al^{3+} has a smaller ionic radius than Cu^{2+} and can induce lattice distortion when incorporated into the host structure. From a crystallographic viewpoint, CuO belongs to the monoclinic crystal system with space group C2/c. For monoclinic CuO, the lattice parameters are typically close to a ≈ 4.68 Å, b ≈ 3.42 Å, and c ≈ 5.13 Å, with the unit-cell angles α = 90°, γ = 90°, and β ≈ 99.5°. Because CuO is not cubic, the relation a = b = c does not apply. Instead, the lattice is distorted, and the monoclinic angle β differs from 90°, which is a key structural feature of tenorite CuO. In Al-doped samples, the basic monoclinic framework is retained, but the slight peak shifts indicate that these lattice parameters may undergo minor changes due to dopant incorporation and the resulting strain. The calculated d-spacing values in Table 1 decrease slightly with increasing Al content, which agrees with the shift of peaks toward higher 2θ values according to Bragg's law. For example, the d-spacing of the first listed peak decreases from 2.7528 Å in S1 to 2.7396 Å in S4, while the d-spacing of the strong peak near 38.7° decreases from 2.3248 Å to 2.3156

Å. This reduction in interplanar spacing confirms that the lattice planes become slightly closer as the Al concentration increases. Such behavior is commonly interpreted as evidence of substitutional doping and internal lattice strain. The full width at half maximum (FWHM) values increase gradually from S1 to S4, while the calculated crystallite size (Dcs) decreases from 17.74 nm for S1 to 15.30 nm for S4 on average. This indicates that Al doping inhibits crystallite growth and promotes smaller coherent diffraction domains. The broadening of peaks in the doped samples also suggests increased lattice disorder and microstrain, both of which are expected when a foreign ion is introduced into the CuO matrix. Therefore, compared with pure CuO, the Al-doped samples are structurally more distorted and slightly less crystalline, especially at higher doping levels. A comparison among the samples shows that S1 has the sharpest peaks, the largest d-spacing values, and the highest average crystallite size, indicating the best crystallinity. S2 shows the beginning of peak shifting and slight broadening, suggesting successful Al incorporation at low concentration. S3 exhibits further peak displacement and narrower d-spacing values, along with a more noticeable reduction in crystallite size. S4 shows the greatest shift toward higher 2θ, the highest FWHM values, and the smallest average crystallite size, indicating the strongest effect of Al doping on the CuO lattice. Thus, the overall trend confirms that increasing Al concentration causes gradual lattice contraction, peak broadening, and crystallite-size reduction while preserving the monoclinic CuO phase [51-55].

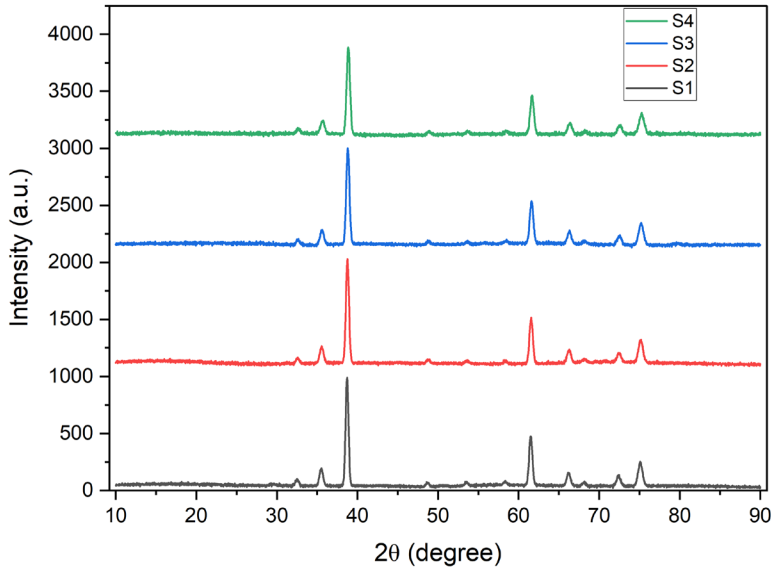

Figure 2 X-ray diffraction (XRD) patterns of pure CuO (S1) and Al-doped CuO samples with different doping concentrations (S2: 1%, S3: 3%, and S4: 5%).

Table 1 Structural parameters of pure and Al-doped CuO nanoparticles (S1–S4) obtained from XRD analysis.

Samples	2θ (°)	FWHM	(hkl)	d-Spacing (Å)	Dcs (nm)	Dcs-ave (nm)
S1	32.50	0.4710	(110)	2.7528	17.57	17.74
	35.50	0.5181	(-111)	2.5267	16.10	
	38.70	0.4239	(111)	2.3248	19.86	
	61.50	0.4710	(-113)	1.5066	19.63	
	66.20	0.5416	(-311)	1.4105	17.51	
	75.10	0.6358	(004)	1.2639	15.76	
S2	32.55	0.4945	(110)	2.7486	16.74	16.90
	35.55	0.5440	(-111)	2.5233	15.34	
	38.75	0.4451	(111)	2.3219	18.92	
	61.55	0.4945	(-113)	1.5055	18.70	
	66.25	0.5687	(-311)	1.4096	16.68	
	75.15	0.6676	(004)	1.2632	15.01	
S3	32.60	0.5181	(110)	2.7445	15.98	16.13
	35.60	0.5699	(-111)	2.5198	14.64	
	38.80	0.4663	(111)	2.3191	18.06	
	61.60	0.5181	(-113)	1.5044	17.85	
	66.30	0.5958	(-311)	1.4087	15.93	
	75.20	0.6994	(004)	1.2625	14.34	
S4	32.66	0.5463	(110)	2.7396	15.15	15.30
	35.66	0.6010	(-111)	2.5157	13.89	
	38.86	0.4917	(111)	2.3156	17.13	
	61.66	0.5463	(-113)	1.5030	16.93	
	66.36	0.6283	(-311)	1.4075	15.11	
	75.26	0.7375	(004)	1.2616	13.60	

3.3. FTIR analysis

The FTIR spectra of pure CuO (S1) and Al-doped CuO samples (S2: 1%, S3: 3%, and S4: 5%) are shown in Figure 3. The spectra exhibit several characteristic absorption bands that confirm the formation of CuO and provide insight into the effect of Al doping on the structural and surface properties of the material. In all samples, a strong absorption band is observed in the low wavenumber region around 500–600 cm^{-1}, which is attributed to the Cu–O stretching vibration. This band confirms the formation of monoclinic CuO. In S1, this peak is sharper and more intense, indicating well-defined Cu–O bonding and higher crystallinity. With increasing Al content (S2, S3, and S4), this band becomes slightly broader and shifts marginally, suggesting lattice distortion and modification of the Cu–O bond due to the incorporation of Al^{3+} ions into the CuO lattice. A noticeable absorption band appears around ~1600 cm^{-1} in all samples, which is assigned to the bending vibration of adsorbed water molecules (H–O–H bending). This indicates the presence of physically adsorbed moisture on the surface of the nanoparticles. The intensity of this band slightly increases with Al doping, implying that Al incorporation enhances surface activity or increases the number of adsorption sites. In the higher wavenumber region, a broad band is observed around ~3200–3500 cm^{-1}, which corresponds to the O–H stretching vibration of hydroxyl groups or adsorbed water. This band becomes more pronounced and broader from S1 to S4, indicating an increase in surface hydroxylation with higher Al concentration. This behavior suggests that Al doping increases surface defects or active sites, facilitating greater interaction with moisture. Additionally, weak bands in the region of ~800–900 cm^{-1} can be attributed to residual nitrate groups or metal–oxygen–metal (M–O–M) vibrations, originating from the precursor materials used in the sol–gel process. These bands diminish slightly with increasing doping, indicating improved decomposition of precursor residues during synthesis and sintering. A comparison among the samples reveals that S1 (pure CuO) shows the least broadening and the lowest intensity of O–H-

related bands, indicating relatively lower surface adsorption and fewer defects. S2 (1% Al) exhibits slight changes in peak intensity and width, confirming initial incorporation of Al into the lattice. S3 (3% Al) shows more pronounced broadening in both Cu–O and O–H bands, suggesting increased lattice distortion and surface activity. S4 (5% Al) demonstrates the most significant changes, including broader Cu–O peaks and stronger O–H absorption, indicating higher defect density, reduced crystallinity, and enhanced surface reactivity [56, 57].

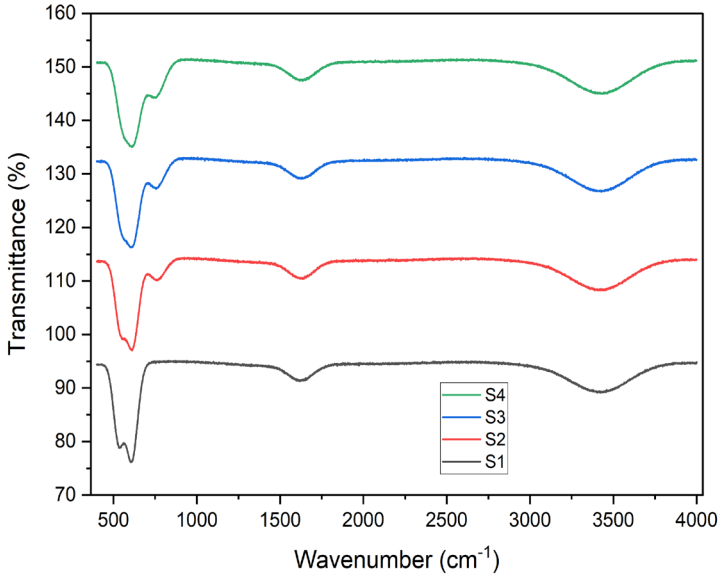

Figure 3 FTIR spectra of pure CuO (S1) and Al-doped CuO NPs with different Al concentrations (S2: 1%, S3: 3%, and S4: 5%).

Table 2 FTIR band assignments for CuO and Al-doped CuO samples.

Samples	Wavenumber (cm^{-1})	Assignment	Description
S1–S4	~500–600	Cu–O stretching	Characteristic vibration of CuO lattice
S1–S4	~800–900	M–O / residual nitrate	Metal–oxygen vibration / precursor remnants
S1–S4	~1500–1650	H–O–H bending	Adsorbed water molecules
S1–S4	~3200–3500	O–H stretching	Surface hydroxyl groups / moisture

3.4. Raman analysis

The Raman spectra of pure CuO (S1) and Al-doped CuO samples (S2: 1%, S3: 3%, and S4: 5%) are presented in Figure 4. The spectra exhibit characteristic vibrational modes corresponding to monoclinic CuO, confirming the phase formation and providing insight into the effect of Al doping on lattice dynamics and structural disorder. For the undoped sample (S1), three prominent Raman peaks are observed around ~290 cm^{-1}, ~340 cm^{-1}, and ~620 cm^{-1}, which are attributed to the Ag and Bg vibrational modes of monoclinic CuO. These peaks are relatively sharp and well-defined, indicating good crystallinity and an ordered lattice structure. The strong peak near ~620 cm^{-1} corresponds to Cu–O stretching vibrations, while the lower wavenumber modes are associated with lattice vibrations involving Cu and O atoms. With the introduction of Al doping (S2, S3, and S4), noticeable changes occur in the Raman spectra. In S2 (1% Al), the Raman peaks remain clearly visible but show slight broadening and minor shifts in peak positions. This suggests that Al^{3+} ions begin to incorporate into the CuO lattice, inducing local lattice distortion without significantly disrupting the crystal structure. As the doping level increases to S3 (3% Al), the Raman peaks become broader and slightly less intense. The peak around ~620 cm^{-1} shows a slight shift and reduction in intensity, indicating increased

lattice strain and disorder. This behavior is attributed to the substitution of Cu^{2+} by Al^{3+} ions, which have a smaller ionic radius, leading to distortion of the CuO lattice and modification of vibrational modes. At the highest doping level, S4 (5% Al), the Raman peaks exhibit the most pronounced broadening and slight shifts. The intensity of the main Cu–O vibration decreases compared to S1, and the peaks become wider, indicating reduced crystallinity and increased structural disorder. The enhanced peak broadening and reduced intensity suggest the presence of lattice defects, micro-strain, and possible phonon confinement effects due to smaller crystallite size, as also supported by XRD results. A comparison among the samples shows that: S1 exhibits the sharpest and most intense peaks, indicating high crystallinity and minimal defects. S2 shows slight peak broadening, indicating initial lattice distortion due to Al incorporation. S3 demonstrates increased disorder and reduced peak intensity. S4 exhibits the highest degree of peak broadening and lowest crystallinity, indicating significant lattice distortion and defect formation. Table 3 summarizes the Raman peak positions and their corresponding vibrational modes for pure and Al-doped CuO samples. The gradual shift and broadening of the Raman bands with increasing Al content indicate enhanced lattice distortion and reduced crystallinity [58].

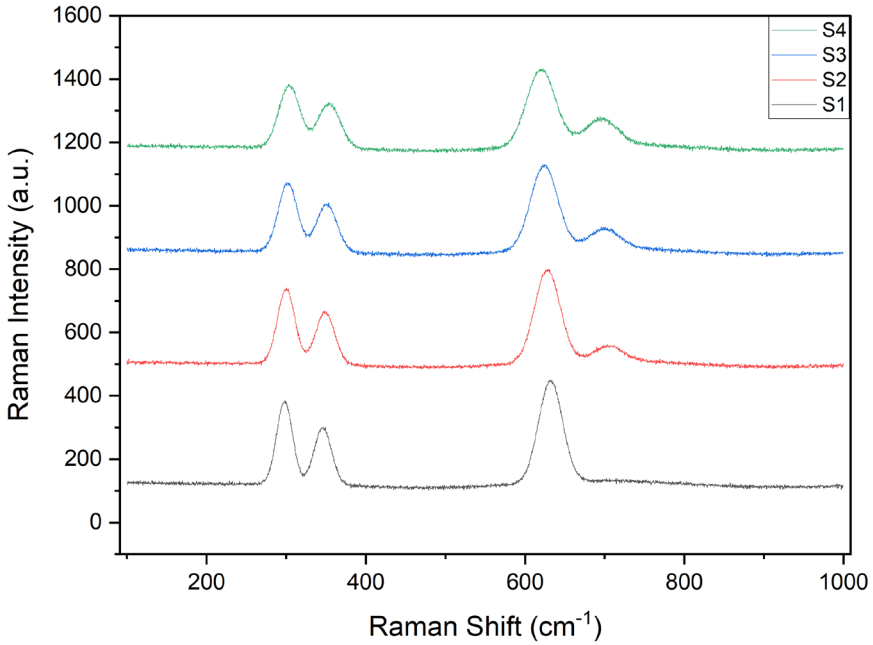

Figure 4 Raman spectra of pure CuO (S1) and Al-doped CuO samples (S2: 1%, S3: 3%, and S4: 5%).

Table 3 Raman peak positions and corresponding vibrational modes of pure CuO (S1) and Al-doped CuO samples (S2–S4).

Samples	Raman shift (cm^{-1})	Vibrational mode / assignment	Interpretation
S1	~298	Ag	Characteristic Raman mode of monoclinic CuO
	~348	Bg	Lattice vibration of CuO
	~633	Bg	Cu–O stretching vibration
S2	~300	Ag	Slightly shifted CuO mode due to Al incorporation
	~351	Bg	Lattice distortion begins with Al doping
	~629	Bg	Cu–O stretching with slight shift/broadening
S3	~302	Ag	Increased shift due to higher Al content
	~353	Bg	Enhanced lattice disorder
	~626	Bg	Broader Cu–O vibration, indicating strain
S4	~304	Ag	Shifted mode due to maximum Al doping
	~356	Bg	Stronger lattice distortion
	~622	Bg	Broadest Cu–O stretching band, indicating reduced crystallinity

3.5. TGA analysis

The thermogravimetric (TGA) curves of pure CuO (S1) and Al-doped CuO samples (S2: 1%, S3: 3%, and S4: 5%) are presented in Figure 5. The weight loss behavior as a function of temperature provides important information about thermal stability, moisture content, and decomposition processes in the samples. As shown in Figure 5, all samples exhibit a gradual decrease in weight with increasing temperature, indicating multi-stage thermal processes. The initial weight loss observed below approximately 150–200°C can be attributed to the removal of physically adsorbed water and surface moisture. Among the samples, S1 (pure CuO) shows the least weight loss in this region, indicating lower moisture adsorption compared to the Al-doped samples. In contrast, S4 (5% Al) exhibits the highest initial weight loss, suggesting that Al doping increases surface activity and enhances the adsorption of moisture, which is consistent with the FTIR results showing stronger O–H bands. In the intermediate temperature range of approximately 200–400°C, a more noticeable weight loss occurs in all samples. This stage is associated with the decomposition of residual organic species and nitrate–citrate complexes originating from the sol–gel synthesis process. The magnitude of weight loss in this region increases with Al content, with S4 showing the highest loss, followed by S3 and S2, while S1 remains the most stable. This indicates that Al incorporation introduces additional lattice defects or residual species that decompose upon heating. At higher temperatures (above ~400°C), the weight loss becomes more gradual and tends to stabilize, indicating the formation of thermally stable CuO structures. However, even in this region, a slight continuous decrease in weight is observed, which may be attributed to the removal of residual impurities and minor structural rearrangements. The pure CuO sample (S1) maintains the highest remaining weight, reflecting superior thermal stability, whereas the Al-doped samples show progressively lower final weights. A comparison among the samples reveals a clear trend: (1) S1 (0% Al) exhibits the highest thermal stability with minimal weight loss. (2) S2 (1% Al) shows moderate weight loss, indicating slight influence of doping. (3) S3 (3% Al) demonstrates increased weight reduction, suggesting more pronounced structural modification. (4) S4 (5% Al) exhibits the highest total weight loss, indicating the greatest degree of lattice distortion and presence of volatile components. The increased weight loss with Al doping can be attributed to several factors, including increased surface area, higher defect density, and enhanced adsorption of moisture and residual species. Additionally, the substitution of Cu^{2+} by Al^{3+} may introduce structural instability at elevated temperatures, leading to increased mass loss. Table 4 shows that the total weight loss increases with increasing Al concentration, confirming enhanced surface adsorption and structural modification in Al-doped CuO samples [59,60].

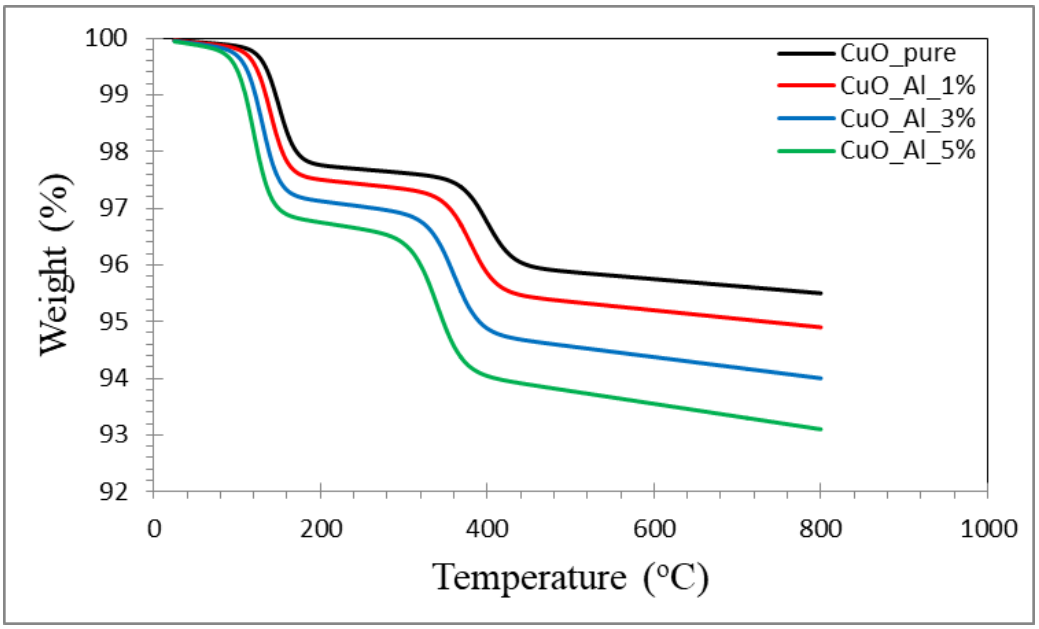

Figure 5 Thermogravimetric analysis (TGA) curves of pure CuO (S1) and Al-doped CuO samples (S2: 1%, S3: 3%, and S4: 5%)

Table 4 Thermal analysis parameters of pure CuO and Al-doped CuO samples obtained from TGA curves.

Samples	Temperature range (°C)	Weight loss (%)	Assigned process	Residual weight (%)
S1 (0% Al)	25–200	~2.2	Removal of adsorbed moisture	
	200–400	~1.6	Decomposition of residual organics/nitrates	
	400–800	~0.7	Structural stabilization	~95.5
S2 (1% Al)	25–200	~2.5	Removal of adsorbed moisture	
	200–400	~1.9	Decomposition of residual organics/nitrates	
	400–800	~0.7	Structural stabilization	~94.9
S3 (3% Al)	25–200	~2.8	Removal of adsorbed moisture	
	200–400	~2.2	Decomposition of residual organics/nitrates	
	400–800	~1.0	Structural stabilization	~94.0
S4 (5% Al)	25–200	~3.1	Removal of adsorbed moisture	
	200–400	~2.6	Decomposition of residual organics/nitrates	
	400–800	~1.3	Structural stabilization	~93.1

3.6. DSC analysis

The DSC curves of pure CuO (S1) and Al-doped CuO samples (S2: 1%, S3: 3%, and S4: 5%) are shown in Figure 6. The curves exhibit distinct endothermic peaks that provide insight into thermal transitions, dehydration processes, and structural changes occurring in the samples. As observed in

Figure 6, all samples display a broad endothermic peak in the low-temperature region around 100–200°C, which is attributed to the removal of physically adsorbed water and surface hydroxyl groups. The intensity of this peak increases with Al content, with S4 showing the most pronounced peak, followed by S3 and S2, while S1 exhibits the least intensity. This behavior indicates that Al doping enhances moisture adsorption and surface activity, consistent with FTIR and TGA results. A second, more prominent endothermic peak appears in the temperature range of approximately 300–400°C for all samples. This peak corresponds to the decomposition of residual organic compounds and nitrate–citrate complexes remaining from the sol–gel synthesis process. In the undoped sample (S1), this peak is relatively sharp and less intense, indicating lower residual content and higher structural stability. However, with increasing Al doping, the peak becomes broader and shifts slightly toward lower temperatures, particularly in S3 and S4, suggesting that Al incorporation facilitates earlier decomposition and introduces structural disorder. Among the samples, S4 (5% Al) exhibits the highest peak intensity and the broadest endothermic feature, indicating the highest energy absorption during decomposition. This suggests increased defect density and a higher amount of residual or unstable species. In contrast, S1 (pure CuO) shows the lowest peak intensity, reflecting better crystallinity and fewer defects. At higher temperatures (above ~400°C), the DSC curves tend to stabilize, indicating that the major thermal events have been completed and the formation of stable CuO phases has occurred. No significant exothermic peaks are observed, confirming the absence of further phase transformations within the studied temperature range. A comparison among the samples reveals that: (1) S1 shows the least intense and sharpest peaks, indicating higher thermal stability and crystallinity. (2) S2 exhibits moderate peak broadening and increased intensity, indicating initial structural modification. (3) S3 shows further peak broadening and shift, reflecting increased lattice distortion. (4) S4 demonstrates the most pronounced endothermic behavior, indicating maximum structural disorder and defect formation. Table 5 presents the DSC peak temperatures and corresponding thermal events of pure and Al-doped CuO samples, highlighting the effect of Al incorporation on thermal behavior [61].

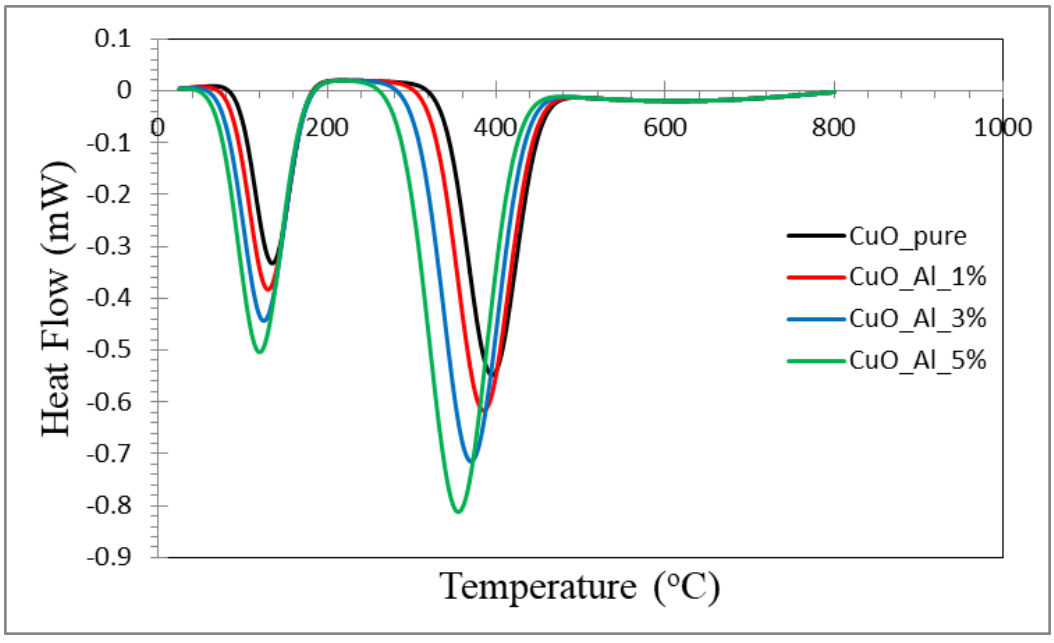

Figure 6 Differential scanning calorimetry (DSC) curves of pure CuO (S1) and Al-doped CuO samples (S2: 1%, S3: 3%, and S4: 5%).

Table 5 DSC thermal parameters of pure and Al-doped CuO samples.

Samples	Peak temperature (°C)	Heat flow (mW)	Thermal event	Interpretation
S1 (0% Al)	~150	~-0.35	Endothermic	Removal of adsorbed moisture
	~360	~-0.55	Endothermic	Decomposition of residual organics
S2 (1% Al)	~145	~-0.40	Endothermic	Moisture removal (enhanced adsorption)
	~350	~-0.60	Endothermic	Decomposition with slight shift
S3 (3% Al)	~140	~-0.45	Endothermic	Increased surface activity
	~340	~-0.70	Endothermic	Enhanced decomposition due to defects
S4 (5% Al)	~135	~-0.50	Endothermic	Highest moisture adsorption
	~330	~-0.80	Endothermic	Maximum structural disorder

3.7. DTG analysis

The derivative thermogravimetric (DTG) curves of pure CuO (S1) and Al-doped CuO samples (S2: 1%, S3: 3%, and S4: 5%) are shown in Figure 7. The DTG analysis provides a more precise identification of the temperatures at which the maximum rate of weight loss occurs, offering deeper insight into the thermal decomposition behavior of the samples. As illustrated in Figure 7, all samples exhibit two main negative peaks, corresponding to two distinct stages of weight loss. The first peak appears in the low-temperature region around 100–200°C, which is associated with the removal of physically adsorbed water and surface-bound hydroxyl groups. The intensity of this peak increases with increasing Al content, with S4 showing the highest peak intensity, followed by S3, S2, and S1. This trend indicates that Al doping enhances moisture adsorption and increases the number of surface-active sites, consistent with FTIR and TGA results. The second prominent DTG peak is observed in the intermediate temperature range of approximately 300–400°C, corresponding to the decomposition of residual organic compounds and nitrate–citrate complexes formed during the sol–gel synthesis process. In the undoped sample (S1), this peak appears at a slightly higher temperature and with lower intensity, indicating greater thermal stability and lower residual content. In contrast, for the Al-doped samples (S2, S3, and S4), the peak shifts slightly toward lower temperatures and becomes more intense, particularly for S4, suggesting that Al incorporation facilitates earlier decomposition and increases structural disorder. A comparison among the samples reveals that: (1) S1 (0% Al) exhibits the lowest peak intensity and highest decomposition temperature, indicating the most thermally stable structure. (2) S2 (1% Al) shows moderate peak intensity and slight peak shift, indicating initial structural modification. (3) S3 (3% Al) demonstrates increased peak intensity and further shift toward lower temperature, reflecting enhanced lattice distortion. (4) S4 (5% Al) exhibits the highest peak intensity and lowest decomposition temperature, indicating maximum defect density and reduced thermal stability. The increase in peak intensity and the shift toward lower temperatures with increasing Al content suggest that Al doping weakens the thermal stability of the CuO lattice by introducing defects and enhancing decomposition kinetics. Additionally, the sharper and more intense DTG peaks in doped samples indicate faster mass loss rates, which may be attributed to increased surface area and higher reactivity [62].

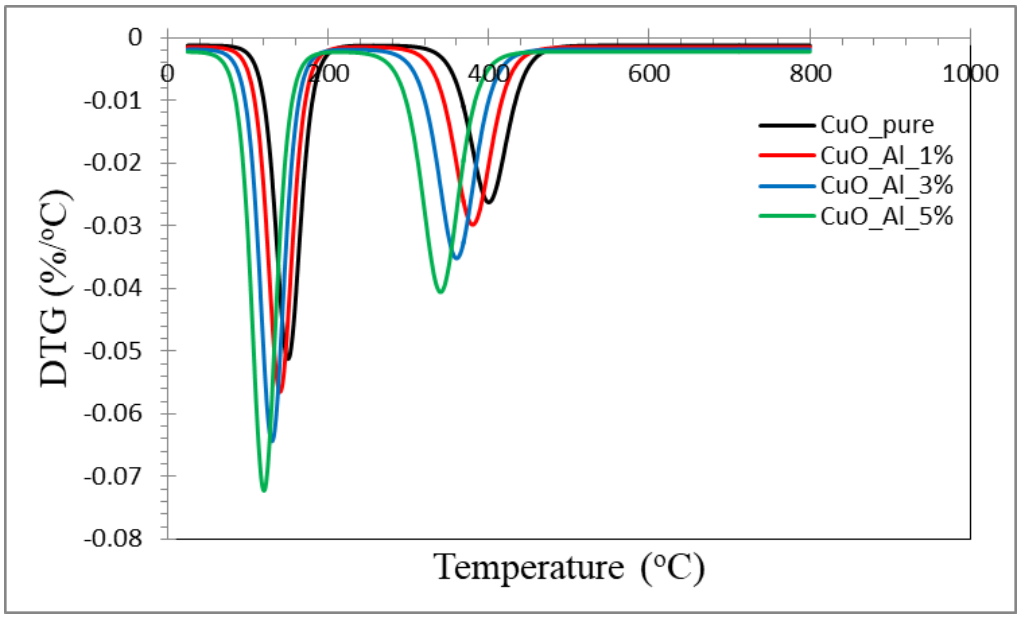

Figure 7 Derivative thermogravimetric (DTG) curves of pure CuO (S1) and Al-doped CuO samples (S2: 1%, S3: 3%, and S4: 5%).

Table 6 DTG peak temperatures and corresponding thermal decomposition stages of pure CuO (S1) and Al-doped CuO samples (S2–S4).

Samples	Peak temperature (°C)	DTG peak (%/°C)	Thermal event	Interpretation
S1 (0% Al)	~150	~-0.05	Moisture removal	Low surface adsorption
	~380	~-0.025	Decomposition	Higher thermal stability
S2 (1% Al)	~145	~-0.055	Moisture removal	Increased adsorption
	~360	~-0.030	Decomposition	Slightly reduced stability
S3 (3% Al)	~140	~-0.065	Moisture removal	Enhanced surface activity
	~350	~-0.035	Decomposition	Increased disorder
S4 (5% Al)	~135	~-0.075	Moisture removal	Maximum adsorption
	~330	~-0.040	Decomposition	Lowest thermal stability

3.8. Evaluation of Al^{3+} ion release from CuO nanoparticles using ICP-OES

The ion release behavior of pure CuO and Al-doped CuO samples is analyzed using ICP-OES, and the results are presented in Figure 8. The data reveal that Al doping significantly influences the ion release characteristics of CuO nanoparticles. As shown in Figure 8, the undoped CuO sample exhibits the highest ion release value of approximately 0.0068 ppm, indicating a relatively higher dissolution rate. This suggests that pure CuO possesses more surface-active sites and weaker structural stability, which facilitates ion leaching into the surrounding medium. Upon doping with 1% Al, the ion release decreases to approximately 0.0052 ppm, demonstrating an improvement in chemical stability. This reduction indicates that the incorporation of Al^{3+} ions strengthen the CuO lattice and reduces the mobility of Cu ions. For the 3% Al-doped sample, the ion release further decreases to about 0.0030 ppm, representing the lowest value among all samples. This suggests that an optimal level of Al doping enhances lattice integrity, minimizes defects, and effectively suppresses ion dissolution. Interestingly, at 5% Al doping, the ion release slightly increases to approximately 0.0038 ppm, although it remains significantly lower than that of pure CuO and the 1% sample. This slight increase may be attributed to excessive doping, which can introduce additional defects or distortions in the

lattice, thereby facilitating limited ion release. A comparison among the samples shows the following trend: CuO (0% Al) → highest ion release, CuO_Al 1% → reduced ion release, CuO_Al 3% → lowest ion release (optimal stability), and CuO_Al 5% → slight increase, but still improved compared to pure CuO. The results indicate that Al doping enhances the chemical stability of CuO nanoparticles, with 3% Al doping providing the most effective reduction in ion release. Beyond this concentration, further doping may introduce structural imperfections that slightly compromise stability.

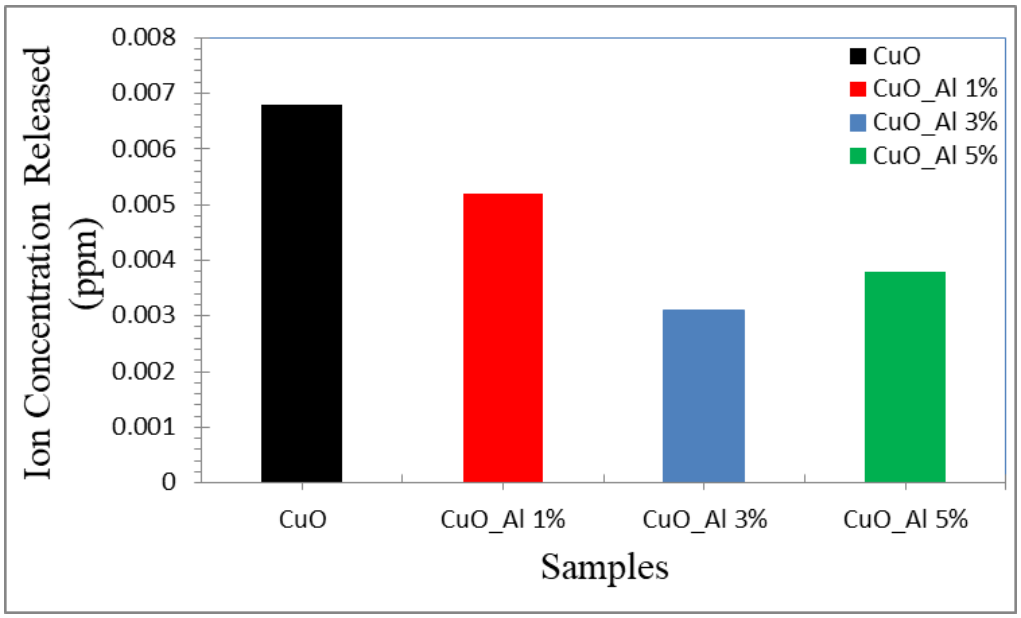

Figure 8 ICP-OES analysis of ion release from pure CuO and Al-doped CuO nanoparticles (1%, 3%, and 5% Al).

4. CONCLUSIONS

In this study, Al-doped CuO nanoparticles with varying Al concentrations (0%, 1%, 3%, and 5%) were successfully synthesized using a citrate-based sol–gel method followed by sintering at 1000 °C. Structural analysis using XRD confirmed that all samples crystallize in the monoclinic CuO phase without the formation of secondary phases, indicating successful incorporation of Al into the CuO lattice. A slight shift in diffraction peaks toward higher 2θ values and a reduction in crystallite size with increasing Al content suggest lattice distortion due to the substitution of Cu^{2+} by smaller Al^{3+} ions. FTIR and Raman analyses further supported the formation of CuO and revealed increased lattice disorder and surface activity with higher Al doping. The broadening of vibrational bands and enhancement of hydroxyl-related features indicate increased defect density and surface adsorption. Thermal analyses (TGA, DSC, and DTG) demonstrated that while all samples exhibit good thermal stability, Al doping slightly reduces thermal stability by promoting earlier decomposition and increasing mass loss, attributed to enhanced surface reactivity and structural defects. The Archimedes measurements showed a significant improvement in densification behavior with increasing Al content, as evidenced by decreasing porosity and increasing bulk density. Additionally, morphological observations revealed that Al doping leads to more uniform and refined particle distribution. The results confirm that Al doping effectively modifies the structural, thermal, and microstructural properties of CuO. Among the studied samples, the 5% Al-doped CuO exhibited the highest densification and surface activity, making it a promising candidate for applications in catalysis, sensing, and electronic devices. Furthermore, the ICP-OES results revealed a composition-dependent variation in ion release behavior, demonstrating an overall decrease in ion release with increasing Al

content, which indicates improved chemical stability of the doped samples. The incorporation of Al^{3+} ions into the CuO lattice enhances structural integrity and reduces ion leaching. However, at higher doping levels (5% Al), a slight increase in ion release was observed compared to the 3% sample, suggesting that excessive doping may introduce additional lattice defects. Overall, Al doping effectively improves the structural, thermal, and chemical stability of CuO nanoparticles without altering their fundamental monoclinic crystal structure. Among all samples, the 3% Al-doped CuO (S3) exhibited the best overall performance, making it a promising candidate for applications requiring enhanced stability and durability.

References

[1] M. M. Najim, B. A. Yousif, The Iraqi Geological Journal 11 (2021) 2 https://doi.org/10.46717/igj.54.1a.3ms-2021-01-24
[2] M. M. Najim, B. A. Yousif, The Iraqi Geological Journal 21 (2020) 49 https://doi.org/10.46717/igj.53.2f.4ms-2020-12-27.
[3] Mojahid Mohammed Najim and Lubna Jaleil Ibraheim, AIP Conference Proceedings 1 (2020) 11 https://doi.org/10.1063/5.0000327
[4] H. M. Abdullah, M. M. Najim, B. A. Yousif, Experimental and Theoretical NANOTECHNOLOGY 9 (2025) 67 https://doi.org/10.56053/9.s.67
[5] H. M. Abdullah, M. M. Najim, B. A. Yousif, Experimental and Theoretical NANOTECHNOLOGY 9 (2025) 39 https://doi.org/10.56053/9.s.39
[6] Ban A.Yousif, Al-œNahrain journal of science 25 (2022) 49 https://doi.org/10.22401/anjs.25.4.08
[7] Al-Hussein, Elham Talib Abd, Yousif, Ban A.. AIP Conference Proceedings, 2213 (2020) 020199 https://doi.org/10.1063/5.0000328
[8] Khalef Wafaa K. et al., International Journal of Nanoelectronics and Materials, 11 (2018) 23 https://doi.org/2-s2.0-85069679313
[9] I. Alshalal, H. M. I. Al-Zuhairi, A. A. Abtan, M. Rasheed, M. K. Asmail. J. Mech. Behav. Mater. 32 (2023) 1 https://doi.org/10.1515/jmbm-2022-0280
[10] M. Sellam, M. Rasheed, S. Azizi, T. Saidani. *Ceram. Int.* 50 (2024) 20917 https://doi.org/10.1016/j.ceramint.2024.03.094
[11] O. Alabdali, S. Shihab, M. Rasheed, T. Rashid. *3rd inter. Scient. conf. alkafeel univ.* (ISCKU 2021) (2022) 39 https://doi.org/10.1063/5.0066860
[12] M. Rasheed, O. Alabdali, S. Shihab, A. Rashid, T. Rashid, J. Phys.: Conf. Ser. 1999 (2021) 012078 https://doi.org/10.1088/1742-6596/1999/1/012078
[13] N. Assoudi et al. Opt. Quant. Electron. 54 (2022) 9 https://doi.org/10.1007/s11082-022-03927-x
[14] R. Jalal, S. Shihab, M.A. Alhadi, M. Rasheed, J. Phys.: Conf. Ser. 1660 (2020) 012090 https://doi.org/10.1088/1742-6596/1660/1/012090
[15] S. Shihab, M. Rasheed, O. Alabdali, A.A. Abdulrahman, J. Phys.: Conf. Ser. 1879 (2021) 22120. https://doi.org/10.1088/1742-6596/1879/2/022120
[16] A. Keziz, M. Heraiz, M. RASHEED, A. Oueslati. Mater Chem. Phys. 325 (2024) 129757 https://doi.org/10.1016/j.matchemphys.2024.129757
[17] D. Kherifi, A. Keziz, M. Rasheed, A. Oueslati. Ceram. Int. 50 (2024) 30175 https://doi.org/10.1016/j.ceramint.2024.05.317
[18] A. Jaber, M. Ismael, T. Rashid, M. A. Sarhan, M. Rasheed, I. M. Sala. Eureka: Phys. Eng. 4 (2023) 29 https://doi.org/10.21303/2461-4262.2023.002770
[19] T. Rashid, M. M. Mokji, M. Rasheed. J. Optics 69 (2024) 47 https://doi.org/10.1007/s12596-024-02080-w
[20] H. K. Aity, E. Dhahri, M. Rasheed. Ceram. Int. 50 (2024) 54666 https://doi.org/10.1016/j.ceramint.2024.10.324

[21] M. Rasheed, S. Shihab, O. Alabdali, A. Rashid, T. Rashid, J. Phys.: Conf. Ser. 1999 (2021) 012077 https://doi.org/10.1088/1742-6596/1999/1/012077
[22] M. Rasheed, M. Nuhad Al-Darraji, S. Shihab, A. Rashid, T. Rashid. J. Phys.: Conf. Ser. 1963 (2021) 012058 https://doi.org/10.1088/1742-6596/1963/1/012058
[23] A. Keziz, M. Heraiz, F. Sahnoune, M. Rasheed, Ceram. Int. 49 (2023) 32989 https://doi.org/10.1016/j.ceramint.2023.07.275
[24] E. Kadri, K. Dhahri, R. Barillé, M. Rasheed. Phase Transi. 94 (2021) 65 https://doi.org/10.1080/01411594.2020.1832224
[25] D. Bouras, M. Rasheed, Opt. Quantum Electron. 54 (2022) 12 https://doi.org/10.1007/s11082-022-04161-1
[26] A. Zubaidi, L.M. Asaad, I. Alshalal, M. Rasheed, J. Mech. Behav. Mater. 32 (2023) 1 https://doi.org/10.1515/jmbm-2022-0302
[27] M. Rasheed et al., J. Phys.: Conf. Ser. 1999 (2021) 012080 https://doi.org/10.1088/1742-6596/1999/1/012080
[28] M. Rasheed, M.N. Al-Darraji, S. Shihab, A. Rashid, T. Rashid, J. Phys.: Conf. Ser. 1963 (2021) 012059 https://doi.org/10.1088/1742-6596/1963/1/012059
[29] M. Enneffatia, M. Rasheed, B. Louati, K. Guidara, S. Shihab, R. Barillé, J. Phys.: Conf. Ser. 1795 (2021) 012050 https://doi.org/10.1088/1742-6596/1795/1/012050
[30] M. Rasheed, O.Y. Mohammed, S. Shihab, A. Al-Adili, J. Phys.: Conf. Ser. 1795 (2021) 012043 https://doi.org/10.1088/1742-6596/1795/1/012043
[31] A.H. Ali, A.S. Jaber, M.T. Yaseen, M. Rasheed, O. Bazighifan, T.A. Nofal, Complexity 2022 (2022) 1 https://doi.org/10.1155/2022/9367638
[32] M. Rasheed, et al., J. Adv. Biotechnol. Exp. Ther. 6 (2023) 495 https://doi.org/10.5455/jabet.2023.d144
[33] M. Rasheed, I. Alshalal, A.A. Ashed, M.A. Sarhan, A.S. Jaber, Indones. J. Electr. Eng. Comput. Sci. 33 (2024) 653 https://doi.org/10.11591/ijeecs.v33.i1.pp653-660
[34] I.M. Mohammed, M. Rasheed, AIP Conf. Proc. 3321 (2025) 020026 https://doi.org/10.1063/5.0289719
[35] F. Boudou, A. Belakredar, A. Berkane, M. Rasheed. Not. Sci. Biol. 17 (2025) 12183 https://doi.org/10.55779/nsb17212183
[36] F. Boudou, et al., Not. Sci. Biol. 17(3) (2025) 12593 https://doi.org/10.55779/nsb17312593
[37] F. Boudou, A. Guendouzi, A. Belkredar. M. Rasheed, Not. Sci. Biol. 16 (2024) 13837 https://doi.org/10.55779/nsb16211837
[38] R.S. Mahmood et al. J. Mech. Behav. Mater. 34 (2025) 1 https://doi.org/10.1515/jmbm-2025-0040
[39] T. Rashid, M.M. Mokji, M. Rasheed, J. Mech. Behav. Mater. 34 (2025) 77 https://doi.org/10.1515/jmbm-2025-0074
[40] M. Rasheed, M. N. Mohammedali, F. A. Sadiq, M. A. Sarhan, T. Saidani. J. Optics (New Delhi. Print) 99 (2024) 89 https://doi.org/10.1007/s12596-024-01928-5
[41] A.J. Hussein, M.N. Al-Darraji, M. Rasheed, M.A. Sarhan, IOP Conf. Ser.: Earth Environ. Sci. 1262 (2023) 022007 https://doi.org/ 10.1088/1755-1315/1262/2/022007
[42] A.J. Hussein, M.N. Al-Darraji, M. Rasheed, M.A. Sarhan, IOP Conf. Ser.: Earth Environ. Sci. 1262 (2023) 022005 https://doi.org/10.1088/1755-1315/1262/2/022005
[43] T. Saidani, M. Rasheed, I. Alshalal, A.A. Rashed, M.A. Sarhan, R. Barillé, Res. Eng. Struct. Mater. 10 (2) (2024) 743 http://dx.doi.org/10.17515/resm2023.21ma0922rs
[44] M. A. Sarhan, S. Shihab, B. E. Kashem, M. Rasheed, J. Phy.: Conf. Ser., 1879 (2021) 022122 https://doi.org/10.1088/1742-6596/1879/2/022122
[45] M. Rasheed, O. Alabdali, S. Shihab, J. Phy.: Conf. Ser. 1879 (2021) 032120 https://doi.org/10.1088/1742-6596/1879/3/032120
[46] M. Rasheed, R. Barillé, J. Non-Cryst. Solids., 476 (2017) 1 https://doi.org/10.1016/j.jnoncrysol.2017.04.027

[47] M. Rasheed, R. Barillé, Opt. Quantum Electron. 49 (2017) 99 https://doi.org/10.1007/s11082-017-1030-7.
[48] F. Dkhilalli, S. M. Borchani, M. Rasheed, R. Barille, K. Guidara, M. Megdiche, J. Mater. Sci. Mater. Electron, 29 (2018) 6297 https://doi.org/10.1007/s10854-018-8609-z.
[49] A. Boumezoued, K. Guergouri, Régis Barillé, Rechem Djamil, Mourad Zaabat, M. Rasheed, J. Alloys Compd. 791 (2019) 550 https://doi.org/10.1016/j.jallcom.2019.03.251
[50] N. Ben Azaza et al., Opt. Mater., 96 (2019) 109328 https://doi.org/10.1016/j.optmat.2019.109328
[51] Areej Adnan Hateef, Essebti Dhahri, M. Rasheed, Habiba Kadhim, Z. Abbas, N. Hassan, Physics and Chemistry of Solid State, 25 (2024) 801 https://doi.org/10.15330/pcss.25.4.801-810
[52] M. Rasheed, SuhaShihab, O. Alabdali, H. H. Hassan, J. Phys. Conf. Ser., 1879 (2021) 032113 https://doi.org/10.1088/1742-6596/1879/3/032113
[53] H. K. Aity, M. Rasheed, E. Dhahri, A. A. Hateef, T. Saidani, Journal of Materials Science, 61 (2026) 6226 https://doi.org/10.1007/s10853-026-12241-w
[54] T. Saidani, S. Mokhtari, M. Rasheed, H. Lahmar, M. Trari, Journal of the Indian Chemical Society, 103 (2026) 102499 https://doi.org/10.1016/j.jics.2026.102499
[55] M. RASHEED, A. Khaleefah, Materials Chemistry and Physics, 353 (2026) 132112 https://doi.org/10.1016/j.matchemphys.2026.132112.
[56] S. S. Batros, M. Rasheed, H. K. Aity, A. A. Hatef, T. Saidani, Materials Chemistry and Physics, 355 (2026) 132243 https://doi.org/10.1016/j.matchemphys.2026.132243
[57] A. Raghdi, M. Heraiz, M. Rasheed, A. Keziz, Journal of the Indian Chemical Society, 101 (2024) 101413 https://doi.org/10.1016/j.jics.2024.101413
[58] A. I. A. Ali, M. RASHEED, Experimental and Theoretical NANOTECHNOLOGY 10 (2026) 277 https://doi.org/10.56053/10.s.277
[59] A. Khaleefah, M. RASHEED, Experimental and Theoretical NANOTECHNOLOGY 10 (2026) 289 https://doi.org/10.56053/10.s.289
[60] Z. S. Ahmed, M. RASHEED, H. S. Ahmed, Experimental and Theoretical NANOTECHNOLOGY 10 (2026) 329 https://doi.org/10.56053/10.s.329
[61] Z. S. Ahmed, M. RASHEED, H. S. Ahmed, Experimental and Theoretical NANOTECHNOLOGY 10 (2026) 343 https://doi.org/10.56053/10.s.343
[62] A. I. A. Ali, M. RASHEED, Experimental and Theoretical NANOTECHNOLOGY 10 (2026) 239 https://doi.org/10.56053/10.s.239